Research

CrossMark
click for updates

Author for correspondence:
P. R. Onck
e-mail: p.r.onck@rug.nl

Royal Society **Publishing**

Numerical modelling of chirality-induced bi-directional swimming of artificial flagella

S. Namdeo[1], S. N. Khaderi[2] and P. R. Onck[1]

[1]Zernike Institute for Advanced Materials, University of Groningen, 9747 AG Groningen, The Netherlands
[2]Department of Engineering, University of Cambridge, Cambridge CB2 1PZ, UK

Biomimetic micro-swimmers can be used for various medical applications, such as targeted drug delivery and micro-object (e.g. biological cells) manipulation, in lab-on-a-chip devices. Bacteria swim using a bundle of flagella (flexible hair-like structures) that form a rotating cork-screw of chiral shape. To mimic bacterial swimming, we employ a computational approach to design a bacterial (chirality-induced) swimmer whose chiral shape and rotational velocity can be controlled by an external magnetic field. In our model, we numerically solve the coupled governing equations that describe the system dynamics (i.e. solid mechanics, fluid dynamics and magnetostatics). We explore the swimming response as a function of the characteristic dimensionless parameters and put special emphasis on controlling the swimming direction. Our results provide fundamental physical insight on the chirality-induced propulsion, and it provides guidelines for the design of magnetic bi-directional micro-swimmers.

1. Introduction

In the modern era of medical science where miniaturized means to perform diagnosis and non-invasive surgery are demanded, micro-swimmers and microbots are a key focus of research and development [1–9]. Many miniaturized externally powered propulsive devices have been suggested that have potential applications in targeted drug delivery and biological cell manipulation in lab-on-a-chip devices [1–11]. As the fundamental challenge lies in achieving a non-reciprocal motion
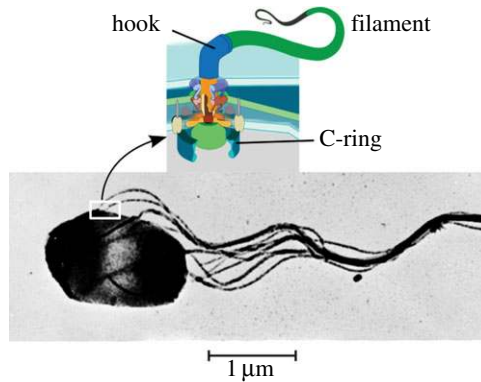
Figure 1. Inspiration from nature: Bacterial swimming using flagella. Electron microscope image of a salmonella bacterium with several flagella forming a bundle of chiral shape (Source: http://www.bmb.leeds.ac.uk/illingworth/6form), where each flagellum is actuated by a base bacterial motor as shown in the inset (Credit: adapted from http://en.wikipedia.org/wiki (File:Flagellum_base_diagram_en.svg)). (Online version in colour.)

at these small length scales [12,13], inspiration can be drawn from nature to design bioinspired artificial micro-swimmers [1,4,5,9–11,14–16]. Bacteria swim using a bundle of flagella (flexible hair-like structures) that form a rotating cork-screw of chiral shape, where each flagellum is actuated by a molecular motor at the bacterial surface, as shown in figure 1. The quest for a simple and viable design of biomimetic bacterial micro-swimmers has attracted considerable attention in the literature [9,13–27]. Various experimental and analytical studies have been performed to analyse the evolution of the chiral shape for an elastic filament or rod-like structure subjected to external actuation [18,19,21–23,25–28]. Also, in an experimental study performed by Garstecki *et al.* [15] a flexible planar structure is deformed into a chiral shape on-the-fly owing to the opposing torques imposed by the externally applied magnetic field and the resisting viscous forces of the surrounding fluid. However, systems that generate chirality 'on-the-fly' do not allow for direction reversal, because the chiral polarity is directly linked to the external actuation. To obtain swimming direction reversal, one has to uncouple the chiral polarity from the external actuation, which can be done by resorting to a pre-manufactured chiral shape. Zhang *et al.* [24] have proposed an elegant procedure that allows manufacturing of a helical belt at the micrometre-scale. However, the manufacturing process involves many more steps compared with systems that feature chirality on-the-fly. This brought us to pose the following question: *Can we achieve propulsion by developing chirality on-the-fly as natural bacteria and still be able to achieve direction-reversal through external actuation*? We address this question in this letter and use a computational approach to magnetically control the chirality of an artificial bacterial micro-swimmer. We investigate the swimming response using dimensionless parameters and explore the underlying physics of the chirality-induced propulsion. We exploit the available physical forces (i.e. elastic, magnetic and viscous) to form the chiral shape on-the-fly and relate the swimming dynamics to the intrinsic competition of these forces. The obtained computational results are supported by analytical expressions derived using resistive force theory [29], which provides the first-order approximation of the swimming velocity.

The article is organized as follows. In §2, we describe the computational model and approach used in this study, where the fluid–solid interaction (FSI) problem is solved by properly accounting for the magnetic forces owing to the external magnetic actuation. Additionally, we identify the dimensionless parameters that govern the swimming dynamics of chirality-induced propulsion. Subsequently, in §3, the results associated with the unidirectional (§3*a*) and the bi-directional (§3*b*) swimming are presented and analysed. Finally, conclusions are drawn that summarize the key points of this work in §4.
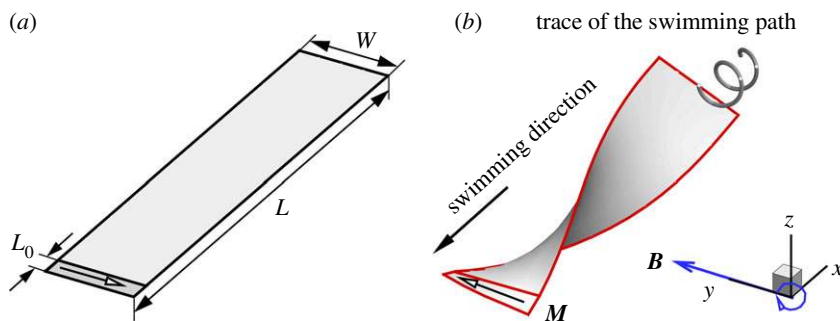
Figure 2. Partially magnetic flexible film subjected to external magnetic actuation (see (*a*)). The dark grey area represents the magnetic portion of the film (L_0) and the arrow indicates the direction of the magnetization (*M*). Propulsion will be achieved by applying an external homogeneous rotating magnetic field (*B*) with a rotation axis along the *x*-axis, and the swimming motion is shown by means of the trace of the swimming path (see (*b*)). Here, the chirality is formed on-the-fly with the help of viscous forces and an animation of unidirectional swimming of such a viscosity-induced chiral shape is included as supplementary material. (See electronic supplementary material at http://dx.doi.org/10.1098/rspa.2013.0547 for the animation of (*a*) unidirectional swimming with the viscosity-induced chiral shape and (*b*) bi-directional swimming with the magnetically induced chiral shape.) (Online version in colour.)

2. Computational model and dimensional analysis

The artificial flagellar micro-swimmer is designed as a planar partially magnetic flexible film that can be easily manufactured with state-of-the-art polymer processing technologies such as inkjet printing (figure 2). The concept exploits the dynamics of a partially magnetic film in which the chiral shape is induced on-the-fly through an externally applied magnetic field. Continuous rotation of such a chiral micro-swimmer leads to a steady-state propulsion subjected to the magnetic actuation (figure 2). To analyse the swimming dynamics of such a chiral micro-swimmer, a computational framework is developed that accounts for the fluid–structure interaction (FSI) between the deforming swimmer and the surrounding fluid, while properly incorporating the changing magnetic forces imposed by the applied magnetic field. We use a finite-element-based framework in which the solid mechanics, fluid dynamics and magnetostatics equations are solved simultaneously. In the model, the micro-swimmer is represented by an assemblage of shell elements, which act as an internal boundary to the fluid domain. The fluid–structure interaction is considered by implicitly coupling the fluid dynamics and solid mechanics equations, where the Stokeslets method is used to account for the viscous environment (and implemented using a boundary-element method). During the simulations, the application of an external magnetic field leads to the generation of magnetic body couples that attempt to align the magnetic portion of the film with the applied magnetic field vector. These magnetic body couples are considered as input (external force vector) to the FSI model. The approach is summarized in appendix A; full details can be found elsewhere [30].

The swimming velocity of the micro-swimmer will depend on the system parameters, such as the geometry and flexibility of the polymer film, viscosity of the aqueous environment, and the magnitude and angular frequency of the applied magnetic field. To explore the influence of each variable on the swimming response of the micro-swimmer, the governing (virtual work) equations can be used to derive a set of characteristic dimensionless numbers that capture the underlying physics of the chirality-induced propulsion,

$$\frac{L_0}{L}, \quad \underbrace{\frac{12\mu\omega}{G}\frac{WL^2}{h^3}}_{F_n\,=\,\text{fluid number}}, \quad \underbrace{\frac{12MB}{G}\frac{LW}{h^2}\frac{L_0}{L}}_{M_n\,=\,\text{magnetic number}}, \tag{2.1}$$

in which L_0/L is a normalized measure of the magnetized region in the polymer film [31] (figure 2), F_n is the fluid number and represents the ratio of viscous forces and elastic forces [31–33] and M_n is the magnetic number and represents the ratio of magnetic forces and elastic forces [31,32]. The derivation of these characteristic dimensionless parameters is given in appendix B. Now, F_n can be independently altered by changing the viscosity (μ) or frequency ($\omega = 2\pi/t_{cycle}$). Similarly, M_n can be independently controlled by changing the remanent magnetization (M) or the external magnetic field (B). Here, we choose the following (fixed) parameters: length (L) = 100 µm, width (W) = 20 µm, thickness (h) = 2 µm, elastic modulus (E) = 490.6 kPa, Poisson's ratio (ν) = 0.3 (giving a shear modulus, G = 188.7 kPa), remanent magnetization (M) = 62.9 kA m^{-1} and viscosity (μ) = 1.0 mPa s^{-1}. The period of the rotating magnetic field (t_{cycle}), magnetic size L_0 and magnitude of the external magnetic field (B) are considered as variables in the analysis.

3. Results and discussion

(a) Unidirectional swimming

Once the partially magnetic flexible film is actuated with a rotating external magnetic field, the chiral shape evolves as a natural consequence of the solid–fluid interaction. The viscous forces of the fluid hinder the motion of the film, while the magnetic portion of the film follows the rotating external magnetic field resulting in opposing torques that forms a twisted ribbon of chiral shape as shown in figure 2. The viscous forces form the chiral shape on-the-fly, which eventually stabilizes leading to a steady-state and unidirectional propulsion subjected to the magnetic actuation (figure 2b).

In figure 3a, we show the swimming velocity as a function of the angular frequency of the applied magnetic field (ω) for three different values of the magnetic field. It can be seen that the velocity increases with frequency until a critical frequency ω_c is reached. This critical frequency increases with increasing magnetic field. Given the definition of the dimensionless numbers (see equation (2.1)), the critical frequency corresponds to a specific critical value of the fluid number, $(F_n)_c$. Here, we can make connection to several experimental studies showing a critical (step-out) frequency ω_c at which the velocity suddenly drops [9,15–17,22,26,27]. In general, ω_c (or, similarly, $(F_n)_c$) quantifies the responsiveness of the system to an externally applied rotating magnetic field. When $F_n > (F_n)_c$, the magnetic micro-swimmer is not able to follow the external magnetic field and starts lagging behind, which results in a tumbling motion and an associated sudden drop of the swimming velocity (figure 3a). The tumbling motion is owing to the fact that when the actuation frequency becomes larger than the critical frequency (i.e. $F_n > (F_n)_c$), the magnetization (M) and external magnetic field (B) vectors are not parallel anymore. Obviously, there is a competition between the magnetic (driving) forces and the viscous (opposing) forces that governs the responsiveness of a magnetic micro-swimmer. In terms of the dimensionless numbers, the ratio of the magnetic forces and viscous forces is represented by $M^* = M_n/F_n \propto MB/\mu\omega$—the inverse of the Mason number [34]—which represent the responsiveness of the magneto-mechanical system. The micro-swimmer will be fully responsive (to the externally applied rotating magnetic field) when the magnetic forces will fully overcome the viscous resistance of the fluid (i.e. when $M^* > M_c^*$).

To further explore the critical responsiveness, we investigate the swimming response of the chiral micro-swimmer solely in terms of the dimensionless numbers F_n and M_n. The normalized swimming velocity as a function of responsiveness of the system ($M^* = M_n/F_n$) for various values of F_n and for $L_0 = 0.1L$ is shown in figure 3b. The swimming velocity (U) is normalized by the factor $\omega W^2/L$ that has been obtained by the first-order calculation based on resistive force theory, [29], which gives

$$U_{analytical} = \frac{\omega\theta_{max}W^2}{12L}\left(\frac{C_{dh}}{C_{dL}} - 1\right),\tag{3.1}$$
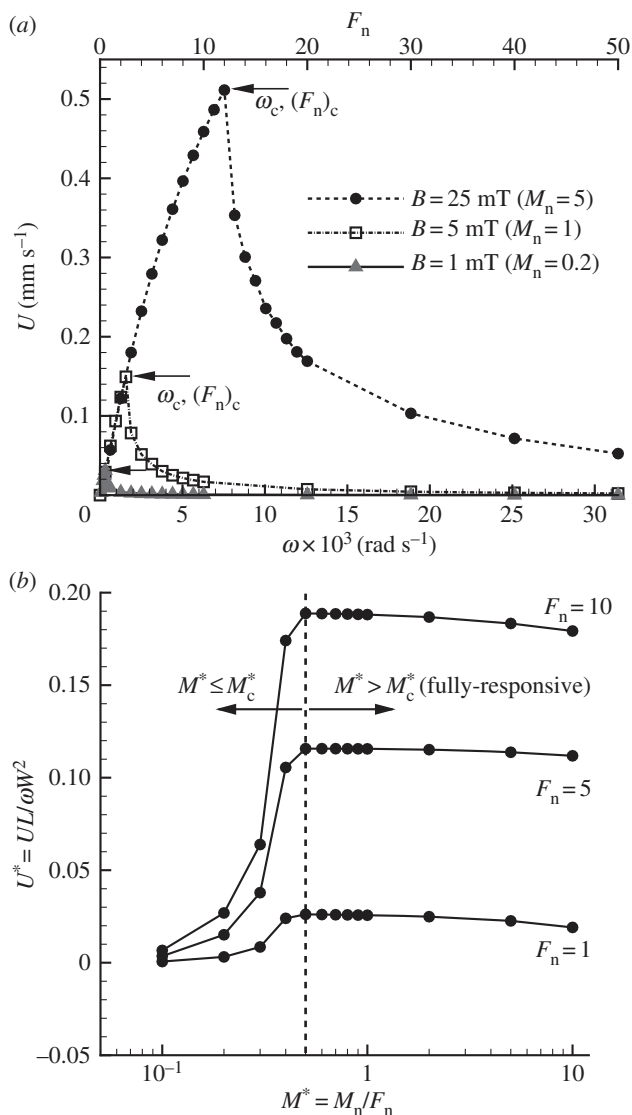
Figure 3. (*a*) Swimming velocity (U) as a function of the angular frequency of the applied magnetic field for various values of B and for $L_0 = 0.1L$. A sudden drop in the swimming velocity is observed at a critical frequency ω_c (or $(F_n)_c$), which is consistent with the experimental observations of step-out frequency for the magneto-responsive systems (see text). (*b*) Normalized swimming velocity as a function of responsiveness of the system ($M^* = M_n/F_n$) for various values of F_n and for $L_0 = 0.1L$. The M^* values only give information about the relative strength of the magnetic forces over the viscous forces, while F_n also captures the ratio of viscous to elastic forces for the micro-swimmer.

where $\theta_{\max}$ is the maximum twist angle present in the film, and C_{dL} and C_{dh} are the local drag-coefficients for a chiral micro-swimmer in the length and thickness direction, respectively (see appendix C for the derivation). For all F_n values, the swimming velocity (U^*) initially increases with M^* followed by a saturation phase and eventually starts decreasing slightly at higher values of M^* (figure 3*b*). The swimming velocity will initially increase as the film starts responding to the external magnetic field (M^* regime between 0 and 0.5), and once the film becomes fully responsive at $M^* \geq M_c^* = 0.5$ (see above in the discussion of figure 3*a*), any further increase in M^* will not get reflected into the corresponding increase in the swimming velocity, and a saturation will be observed.
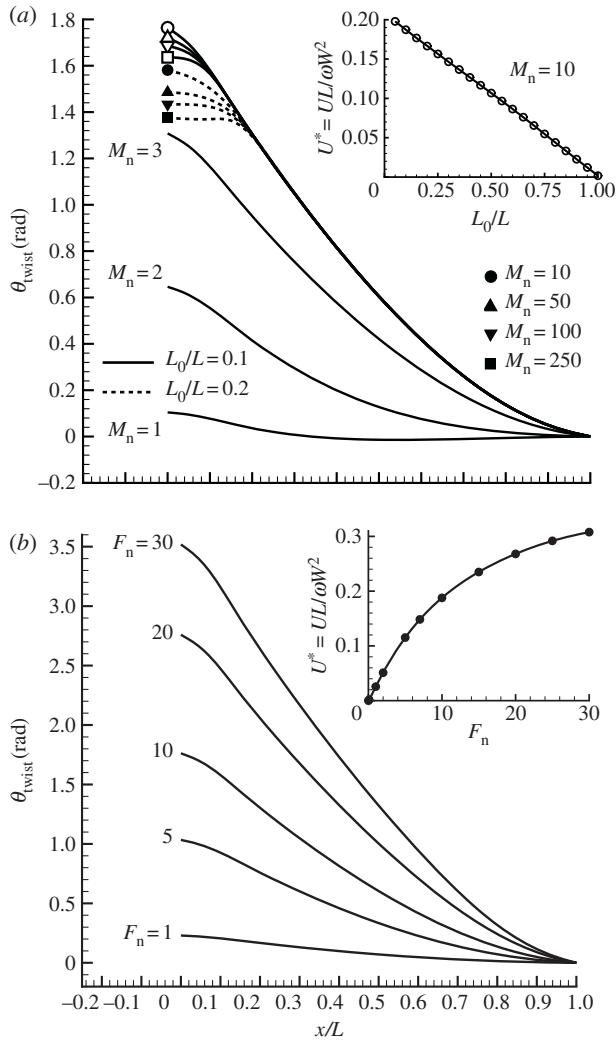
Figure 4. (*a*) Twist angle variation along the micro-swimmer length as a function of M_n for $F_n = 10$. The maximum twist angle at $x = 0$ (θ_{max}) increases with M_n initially. However, at higher M_n values the magnetic portion (L_0) of the film becomes difficult to deform and causes a reduction of θ_{max} (and a corresponding decrease of the swimming velocity; figure 3*b*). This effect is more prominent for higher values of L_0/L and the influence of L_0/L on the swimming velocity for $F_n = 10$ and $M^* = 1$ is shown in the inset, where ($L - L_0$) quantifies the available length of the micro-swimmer to form a chiral shape. (*b*) Variation of the twist angle along the length as a function of F_n for $M^* = 1$ and $L_0 = 0.1L$. For a fully responsive micro-swimmer θ_{max} increases with F_n, which leads to an enhancement of the swimming velocity as shown in the inset.

The analytical expression for the velocity based on the resistive force theory (equation (3.1)) holds for a constant helicity along the swimmer and shows that the swimming velocity is directly proportional to the maximum twist angle (θ_{max}) accommodated by the film. In the numerical simulations, however, owing to the elastic and magnetic interactions with the viscous fluid, the twist angle distribution becomes nonlinear. We therefore did not include θ_{max} in the normalization for U. To explore the relationship between twist angle and applied magnetic field, we analyse the twist angle variation along the length of the film as a function of M_n for $F_n = 10$, $L_0 = 0.1L$ (figure 4*a*). It can be clearly seen that the twist angle for lower values of M_n ($M^* < M_c^* = 0.5$) is limited as the film is not able to overcome the fluid's resistance. The twist angle increases with M_n and eventually attains a saturation at higher values of M_n when the film becomes fully

responsive (i.e. $M^* \geq M_c^* = 0.5$). Note that the maximum twist angle (θ_{max}) accommodated by the film depends on the magnitude of the viscous forces (related to F_n) and will be discussed later. Interestingly, higher values of M_n result into reducing the twist angle variation inside the magnetic portion of the film and eventually reduce θ_{max}, which explains the slight decrease in swimming velocity for large M_n values as shown in figure 3b. This is a natural consequence of the external magnetic torque acting only on the magnetic portion of the film, which ultimately restrains the deformation of the magnetic part of the film at higher M_n values, and causes the magnetic portion to behave as rigid. Note that this effect becomes more prominent for higher values of L_0/L as shown in figure 4a. For a fully responsive micro-swimmer ($M^* \geq 0.5$), the influence of the magnetic portion L_0/L on the swimming velocity is shown in the inset of figure 4a. As L_0/L also quantifies the availability of the micro-swimmer's length to form a chiral shape, the swimming velocity is linearly dependent on L_0/L. $L_0/L = 0$ and 1 represent the extreme cases for the magnetic portion and in both cases the swimming velocity will be zero owing to either the absence of external actuation ($L_0 = 0$) or reciprocal motion of the film ($L_0 = L$). Next, we study the effect of viscous forces in the limit of fully responsive micro-swimmers ($M^* = 1$). The response of the twist angle variation along the micro-swimmer length as a function of F_n (for $M^* = 1$) is shown in figure 4b. The maximum twist angle increases with F_n which leads to an increase in the swimming velocity, as shown in the inset. Increasing F_n at constant M^* physically corresponds to decreasing the stiffness of the micro-swimmer. This leads to an increasing twist angle, and thus an increasing velocity (inset), in correspondence with equation (3.1).

(b) Bi-directional swimming

Direction reversibility is a desirable feature for object manipulation in confined flow geometries, such as in the human arterial system and in miniaturized lab-on-a-chip devices. The approach studied in the previous section of forming a chiral shape on-the-fly by exploiting the viscous forces, severely reduces the manufacturing demands for a bacterial micro-swimmer. However, it does not have the possibility to change/reverse swimming direction. To achieve swimming bi-directionality, we suggest to magnetically control the initial chirality through two magnetic sections with opposite remanent magnetization (figure 5). Here, (controlled or non-controlled) manufacturing imperfections will serve as a perturbation to the system resulting in an initial chiral shape when the film is brought under the influence of an external magnetic field (figure 5) and swimming can be achieved by subsequently rotating the magnetic field. As the chiral shape is now independent of the rotation direction of the magnetic field, forward and backward swimming can be triggered by inverting the rotation direction. Note that the twist angle (chirality) is now explicitly induced through the initial application of the external magnetic field and has an upper limit of 180° (figure 5).

The dependence of the swimming velocity (U^*) on the responsiveness of the system ($M^* = M_n/F_n$) for various values of F_n and for $L_0/L = 0.05L$ is shown in figure 6a. For all F_n values, the swimming velocity increases initially with M_n as the system responds to the externally applied magnetic field and eventually saturates at higher M^* values. Again, any increase in the M_n value directly increases the initial twist angle in the film (as the film becomes more responsive). The upper limit for the twist angle (180°) is reached at relatively high M^* values leading to a saturation in the swimming velocity (as $U \propto \theta_{max}$, see equation (3.1)). Note that the lower velocities for $M^* < 100$ are not owing to the 'slipping' or 'tumbling' motion observed for the previous system (figure 3), but is entirely owing to the elastic resistance that limits the twist angle. The influence of L_0/L on the swimming velocity is linear (see inset of figure 6a), which is owing to the fact that the magnetized portion of the film does not contribute to the chiral shape formation as it behaves as rigid under the influence of the large external magnetic field. It is worth mentioning that there are two significant differences in the new approach; first, the swimming velocity saturates at relatively high M^* values ($M^* > 100$[1]), and second the swimming velocity

---

[1]For this study, aspect ratio (L/W) of the film is 5. For larger aspect ratios of the film, the M^* value required for the saturation in the swimming velocity will be less as the twist angle (for a given external torque) $\theta \propto L/W$.
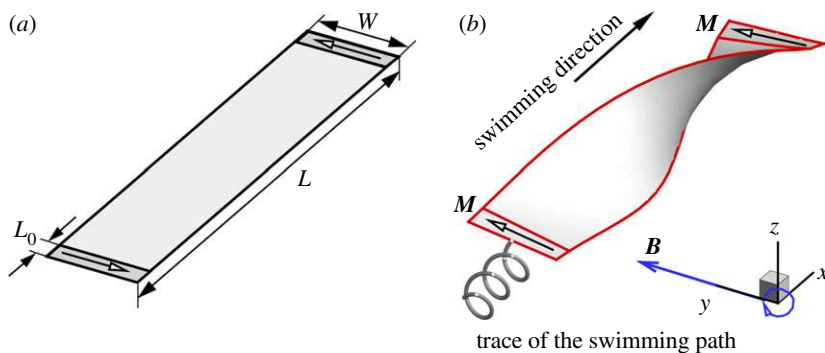
Figure 5. Partially magnetic flexible polymer film where the dark grey areas represent the magnetic portions of the film (L_0) and the arrows indicate the direction of the respective magnetization **M** (see (*a*)). The chiral shape is formed by a static external magnetic field and the swimming is achieved by subsequently rotating the magnetic field with a rotation axis along the *x*-axis (see (*b*)). An animation of bi-directional swimming with a magnetically induced initial chiral shape is included as electronic supplementary material. (See electronic supplementary material at http://dx.doi.org/10.1098/rspa.2013.0547 for the animation of (1) unidirectional swimming with a viscosity-induced chiral shape and (2) bi-directional swimming with a magnetically induced chiral shape.) (Online version in colour.)

does not go to zero when the film becomes fully magnetic ($L_0/L = 0.5$) owing to the novel design of the micro-swimmer, where both (end) magnetic portions are used to form the chiral shape.

We further explore the influence of F_n on the swimming velocity for a fully responsive system ($M_n \propto F_n$) as shown in figure 6*b*. The swimming velocity increases with F_n initially and then saturates, which is followed by small dip at large F_n values. The initial trend can be explained by the corresponding increase in M_n that increases the induced initial chirality (θ_{max}) in the micro-swimmer. However, the observed dip at higher F_n values is related to the change in the twist angle distribution along the micro-swimmer length as shown in the inset of figure 6*b* for various values of F_n. It can be clearly seen that at higher F_n values the steady-state chirality distribution is different from what is initially induced. The large viscous forces of the fluid at higher F_n values start deforming the magnetically induced (initial) chiral shape, which results in a nonlinear distribution of chirality along the micro-swimmer length instead of a linear distribution induced initially. We have analysed the effect of nonlinearity by assuming a power-law relationship for the twist angle variation, $\theta = \theta_{max}(x/L)^n$ (see appendix C). Analytical results based on resistive force theory show that the swimming velocity is maximal for a linear distribution of twist angle along the micro-swimmer length ($n = 1$), see appendix C.

Finally, the two suggested concepts to obtain a chiral shape (viscosity-induced or magnetically induced) can be compared. The swimming response associated with these concepts as a function of the fluid number F_n is shown in figure 7 for the fully responsive systems. Note that the magnetically induced chirality concept should be preferred as (i) it facilitates bi-directionality in the swimming direction and (ii) the swimming velocity remains independent of the fluid number (F_n), which allows operational accommodation of different fluid viscosities (μ) and allows tuning the applied frequency ω, given that the magnetic number (M_n) is large enough to overcome the elastic resistance of the film and form a chiral shape. It is advisable to increase the length of the magnetized portion (L_0/L) to reduce the deformations owing to the viscous force at higher F_n values. The micro-swimmers can be fabricated with ink-jet printing or photolithography [35–38] by using magnetic nanoparticles for the two magnetic domains. However, fabricating a film with two ends magnetized in opposite directions is not straightforward. A two-step manufacturing procedure would be required using two opposing directions of the applied magnetization field in each step. The opposing polarities are established by shielding one end in the first step and the other end in the second.
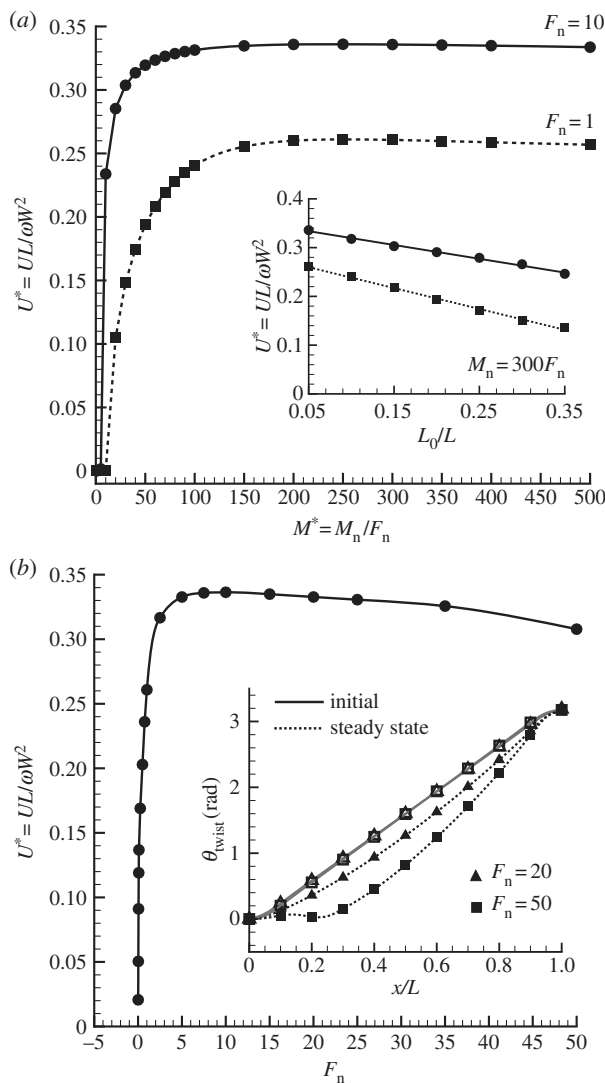
Figure 6. (*a*) Swimming velocity as a function of responsiveness of the system ($M^* = M_n/F_n$) for two values of F_n (1 and 10) and for $L_0 = 0.05L$. Influence of L_0/L on the swimming velocity for a fully responsive system ($M_n = 300F_n$) is shown in the inset. The circles correspond to $F_n = 10$ and the squares to $F_n = 1$. (*b*) Swimming velocity as a function of F_n for a fully responsive system ($M_n = 300F_n$) and for $L_0 = 0.05L$. Chirality distribution along the micro-swimmer length as a function of F_n is shown in the inset. At higher values of F_n, the magnetically formed initial chiral shape starts deforming during swimming, which causes a reduction in the swimming velocity at higher F_n values.

4. Summary and conclusion

Artificial micro-swimmers can potentially be used for various bio-medical applications, such as micro-object manipulation on lab-on-a-chip devices and for targeted drug delivery. A bioinspired approach has been taken by mimicking bacterial swimming through magnetically driven chirality-induced propulsion. We have used a computational approach based on a functional polymer film whose chiral shape and rotational velocity are controlled by a rotating magnetic field. Furthermore, we have identified the key dimensionless parameters of the chirality-induced propulsion and investigated the competition between elastic, viscous and magnetic forces that are responsible for the physical response. The suggested bacterial micro-swimmers form a chiral
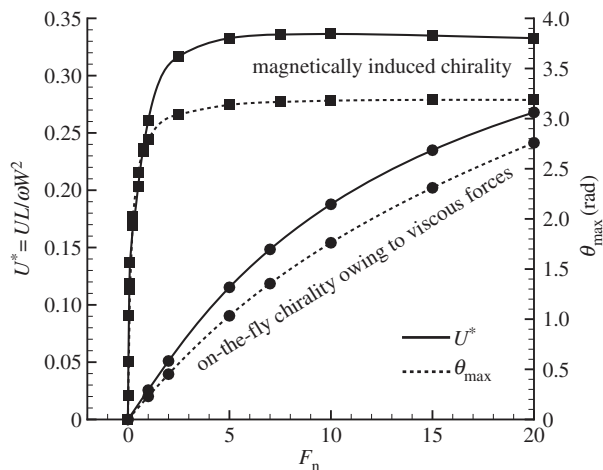
Figure 7. Swimming response (and the twist angle accommodated by the film) as a function of the fluid number F_n for the fully responsive systems. The magnetically induced chiral system corresponds to figure 2 and the 'on-the-fly' chiral system to figure 5. The solid and dashed lines represent the swimming velocity and the twist angle, respectively. The swimming velocity is linearly dependent on the twist angle.

shape on-the-fly (from an initial planar geometry) by exploiting the available physical forces (i.e. elastic, magnetic and viscous). In this on-the-fly system, viscous forces are used to induce a chiral shape during swimming. However, this does not permit bi-directionality. To overcome this, a new concept is proposed that uncouples the chiral-polarity from the external actuation by forming an initial chiral shape through two magnetic sections with opposite remanent magnetization. Forward and backward swimming can be achieved by tuning the rotation direction of the magnetic field. The micro-swimmer—a planar functional polymer film—can be easily manufactured with state-of-the-art polymer processing technologies such as inkjet printing, and opens possibilities for various bio-medical applications such as micro-object manipulation in lab-on-a-chip devices.

Appendix A. Computational model

To solve the coupled FSI involved in the swimming of bacterial flagella, we use a three-dimensional computational framework in which the solid mechanics, fluid-dynamics and magneto-static equations are solved simultaneously. By implicitly coupling the solid mechanics and fluid dynamics equations, we incorporate the equivalent drag matrix owing to the fluid into the stiffness matrix. The magnetic body couples acting on the micro-swimmer owing to external magnetic-actuation is computed on-the-fly and supplied to the FSI model as an external force vector. Here, we briefly summarize the computational framework; for full details of the approach, the reader is referred to Khaderi & Onck [30].

(a) Magnetostatics

The magneto-responsive micro-swimmers are subjected to magnetic body couples (N) owing to the externally applied magnetic field (B), which can be obtained from the cross-product of the film remanent magnetization (M) and the external magnetic field, $N = M \times B$. The magnetic body couples (N) are considered as input to the FSI model and supplied as an external force vector
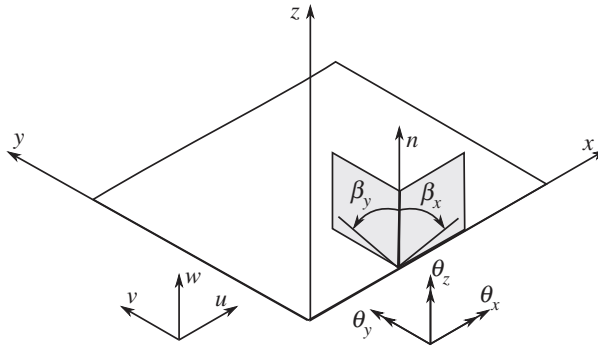
Figure 8. Illustration of the parameters involved in the shell element formulation [30].

[30], see equation (A 12). Magnetic interactions between multiple magnetic domains are assumed to be small and are therefore not accounted for.

(b) Finite-element formulation for the solid mechanics equations

The micro-swimmer is represented by an assemblage of shell elements, which can undergo large deformation. For the shell elements, the displacement of any point on the normal can be written in terms of the displacements on the mid-surface (u_0, v_0, w_0)

$$u = u_0 + z\beta_x, \quad v = v_0 - z\beta_y, \quad w = w_0, \tag{A 1}$$

where β_x and β_y are the rotations of the normal with respect to the x- and y-axes, respectively, as indicated in figure 8. The associated non-zero components of the Green–Lagrange strain are

$$\epsilon_x = \frac{\partial u}{\partial x} + \frac{1}{2}\left(\frac{\partial w}{\partial x}\right)^2, \quad \epsilon_y = \frac{\partial v}{\partial y} + \frac{1}{2}\left(\frac{\partial w}{\partial y}\right)^2 \quad \text{and} \quad 2\epsilon_{xy} = \frac{\partial u}{\partial y} + \frac{\partial v}{\partial x} + \frac{\partial w}{\partial x}\frac{\partial w}{\partial y}. \tag{A 2}$$

The variation of these Green–Lagrange strains can be obtained in terms of the axial strain $\bar{\epsilon}$ and the curvature κ using the displacement definitions given in equation (A 1)

$$\delta\epsilon_x = \frac{\partial \delta u}{\partial x} + \frac{\partial w}{\partial x}\frac{\partial \delta w}{\partial x} = \underbrace{\frac{\partial \delta u_0}{\partial x} + \frac{\partial w_0}{\partial x}\frac{\partial \delta w_0}{\partial x}}_{\text{axial strain}} + \underbrace{z\frac{\partial \delta\beta_x}{\partial x}}_{\text{curvature}} = \delta\bar{\epsilon}_x + z\delta\kappa_x. \tag{A 3}$$

Similarly,

$$\delta\epsilon_y = \delta\bar{\epsilon}_y + z\delta\kappa_y \quad \text{and} \quad 2\delta\epsilon_{xy} = \delta\bar{\epsilon}_{xy} + z\delta\kappa_{xy}. \tag{A 4}$$

The internal virtual work can be written as

$$\delta W_{\text{int}} = \int_{V_0} (\sigma_x \delta\epsilon_x + \sigma_y \delta\epsilon_y + 2\sigma_{xy}\delta\epsilon_{xy})\, dV, \tag{A 5}$$

where σ_x, σ_y and σ_{xy} are the components of the second Piola–Kichhoff stress tensor and dV represents an elemental volume in the undeformed configuration. Assuming the shell elements of uniform cross section with thickness h, we can write the above equation using an elemental area dA in the undeformed configuration as

$$\delta W_{\text{int}} = \int_{A_0} (\delta\boldsymbol{\epsilon} \cdot \boldsymbol{P} + \delta\boldsymbol{\kappa} \cdot \boldsymbol{M})\, dA, \tag{A 6}$$

where $\boldsymbol{\epsilon} = [\bar{\epsilon}_x\ \bar{\epsilon}_y\ \bar{\epsilon}_{xy}]^{\text{T}}$, $\boldsymbol{\kappa} = [\kappa_x\ \kappa_y\ \kappa_{xy}]^{\text{T}}$, and $\boldsymbol{P}$ and $\boldsymbol{M}$ are the associated membrane forces and bending moments, respectively [30]. The internal virtual work at time $t + \Delta t$ can be written as

$$\delta W_{\text{int}}^{t+\Delta t} = \int_{A_0} (\delta\boldsymbol{\epsilon}^{t+\Delta t} \cdot \boldsymbol{P}^{t+\Delta t} + \delta\boldsymbol{\kappa}^{t+\Delta t} \cdot \boldsymbol{M}^{t+\Delta t})\, dA, \tag{A 7}$$

which can be expanded linearly in time by assuming $Q^{t+\Delta t} = Q^t + \Delta Q$, and can be simplified by neglecting the higher order terms, leading to

$$\delta W_{\text{int}}^{t+\Delta t} = \int_{A_0} (\delta \boldsymbol{\epsilon}^t \cdot \boldsymbol{P}^t + \delta \boldsymbol{\kappa}^t \cdot \boldsymbol{M}^t + \Delta \delta \boldsymbol{\epsilon} \cdot \boldsymbol{P}^t + \delta \boldsymbol{\epsilon}^t \cdot \Delta \boldsymbol{P} + \delta \boldsymbol{\kappa}^t \cdot \Delta \boldsymbol{M}) \, \mathrm{d}A. \tag{A 8}$$

We use the finite-element formulation to discretize the system in terms of the nodal displacements (u, v, w) and rotations $(\theta_x, \theta_y, \theta_z)$ of three-noded triangular elements with

$$\boldsymbol{d}_e = [u_1 \; v_1 \; w_1 \; \theta_{x1} \; \theta_{y1} \; \theta_{z1} \; u_2 \; v_2 \; w_2 \; \theta_{x2} \; \theta_{y2} \; \theta_{z2} \; u_3 \; v_3 \; w_3 \; \theta_{x3} \; \theta_{y3} \; \theta_{z3}]^{\mathrm{T}}, \tag{A 9}$$

where the subscripts 1, 2 and 3 denote the respective three nodes of the element.

To capture the deformation of the films, both the bending and membrane stiffnesses (stiffness associated with the in-plane stretching) have to be accurately modelled. To do so, we adopt the approach proposed by Bathe & Ho [39] and model the bending of the films using discrete Kirchhoff triangles, while the membrane behaviour is accounted for using constant strain triangles (CSTs) [30]. To improve the accuracy during in-plane bending, we add drilling degrees of freedom to the CSTs [40], and adopt an updated Lagrangian framework to arrive at the final set of equations. The resulting stiffness matrix includes the geometric nonlinearity, which accounts for large deformations but small strains [30], see below.

$$\delta W_{\text{int}}^{t+\Delta t} = (\delta \boldsymbol{d}_e)^{\mathrm{T}} \boldsymbol{f}_{\text{int}}^t + (\delta \boldsymbol{d}_e)^{\mathrm{T}} (\boldsymbol{k}_{\text{M}}^t + \boldsymbol{k}_{\text{G}}^t) \Delta \boldsymbol{d}_e, \tag{A 10}$$

where $\boldsymbol{k}_{\text{M}}$ is the material stiffness matrix, $\boldsymbol{k}_{\text{G}}$ is the geometric stiffness matrix and $\boldsymbol{f}_{\text{int}}$ is the internal force vector [30]. After performing the standard finite-element assembly and coordinates transformation (local-to-global), we obtain

$$\delta W_{\text{int}}^{t+\Delta t} = \delta \boldsymbol{d}^{\mathrm{T}} \boldsymbol{F}_{\text{int}}^t + \delta \boldsymbol{d}^{\mathrm{T}} (\boldsymbol{K}_{\text{M}}^t + \boldsymbol{K}_{\text{G}}^t) \Delta \boldsymbol{d}. \tag{A 11}$$

The external virtual work at time $t + \Delta t$ can be written as

$$\delta W_{\text{ext}}^{t+\Delta t} = \int_V (-N_x \delta \beta_y + N_y \delta \beta_x) \, \mathrm{d}V_{\text{m}}, \tag{A 12}$$

where N_x and N_y are the externally applied magnetic body couples (see appendix Aa), and V_{m} is the magnetic portion of the film. After discretization and the standard finite-element assembly procedure, the external virtual work can be written as [30]

$$\delta W_{\text{ext}}^{t+\Delta t} = \delta \boldsymbol{d}^{\mathrm{T}} \boldsymbol{F}_{\text{ext}}^{t+\Delta t}. \tag{A 13}$$

(c) Boundary-element formulation for the fluid dynamics equations

For the fluid we make use of the Stokeslet approach in which the force exerted on the fluid at the surface of the solid structure is approximated by the distribution of Stokeslets along the length of the structure. The velocity and force fields are related by a Green's function that has a singularity proportional to $1/r$ in three dimensions [41]. The expression of Green's function $(\boldsymbol{G})$ for the Stokeslets relates the velocity at location $\boldsymbol{r}, \dot{\boldsymbol{u}}$, to the forces at location $\boldsymbol{r}', \boldsymbol{f}$, through

$$\dot{\boldsymbol{u}} = \boldsymbol{G} \boldsymbol{f} \quad \text{and} \quad G_{ij} = \frac{1}{8\pi\mu} \left\{ \frac{\delta_{ij}}{R} + \frac{R_i R_j}{R^3} \right\} \quad (i, j = 1, 2, 3), \tag{A 14}$$

where $\boldsymbol{R} = \boldsymbol{r} - \boldsymbol{r}'$, $R = |\boldsymbol{R}|$ is the distance between the two locations $\boldsymbol{r}$ and $\boldsymbol{r}'$, and δ_{ij} is the Kronecker delta. By assuming the point force $\boldsymbol{f}$ to be represented by the traction $\boldsymbol{f} = \boldsymbol{T} \, \mathrm{d}S$ over the solid surface, the boundary-integral equation can be written as

$$\dot{\boldsymbol{u}} = \int_{\text{boundary}} \boldsymbol{G} \boldsymbol{T} \, \mathrm{d}S = \sum_{\text{nelm}} \int_S \boldsymbol{G} \boldsymbol{T} \, \mathrm{d}S = \sum_{\text{nelm}} \int_S \boldsymbol{G} \boldsymbol{N} \, \mathrm{d}S \boldsymbol{t}, \tag{A 15}$$

where T are the tractions imposed on the fluid [33]. In equation (A 15), the boundary-integral equation has been discretized using boundary elements (three-noded shell elements), and the tractions are linearly interpolated using $T = Nt$ with t being the tractions at the nodes. When equation (A 15) is used to evaluate the velocity in all nodes of the micro-swimmer, we obtain a system of equations $\dot{U} = G_f t$ that relates the traction t exerted by the micro-swimmer on the fluid to its velocity $\dot{U}$. The integration procedure is adopted from the literature, where the singular integrals are evaluated using the method of change of variables [41] and the non-singular integrals are evaluated using standard two-dimensional Gaussian Quadrature [30]. Once the velocity of the solid surface is known, this relation can be inverted to obtain the nodal tractions [33]: $t = G_f^{-1}\dot{U}$.

(d) Fluid–solid interaction and implicit coupling

Coupling of the solid mechanics and fluid dynamics equations will be done in an implicit manner by incorporating the equivalent drag matrix owing to the fluid into the stiffness matrix. The external virtual work owing to the fluid's drag forces (T_d) can be given as

$$
\delta W_{\text{fluid}}^{t+\Delta t} = \int (\delta u)^{\text{T}} T_d^{t+\Delta t} \, dS = - \int (\delta u)^{\text{T}} N \, dS t^{t+\Delta t}
$$

$$
\approx -(\delta d_e)^{\text{T}} \int N^{\text{T}} N \, dS t^{t+\Delta t} = -(\delta d_e)^{\text{T}} M_e t^{t+\Delta t}, \tag{A 16}
$$

where $M_e = \int N^{\text{T}} N \, dS$, u is the displacement vector, and d_e is the local nodal displacement vector [30]. Note that the minus sign appears because of the change of reference (from fluid to the structure, $T_d = -T$). After performing the standard finite-element assembly procedure, we obtain

$$
\delta W_{\text{fluid}}^{t+\Delta t} = -(\delta d)^{\text{T}} M t^{t+\Delta t} = -(\delta d)^{\text{T}} M G_f^{-1} \dot{U}^{t+\Delta t}, \tag{A 17}
$$

where the matrix G_f relates the velocity of the solid structure to the traction, see the end of the previous subsection. Now, using the no-slip boundary condition $\dot{U} = A \Delta d / \Delta t$ it follows that

$$
\delta W_{\text{fluid}}^{t+\Delta t} = -(\delta d)^{\text{T}} \frac{M G_f^{-1} A \Delta d}{\Delta t} = -(\delta d)^{\text{T}} K_{\text{D}}^t \Delta d, \tag{A 18}
$$

where $K_{\text{D}} = M G_f^{-1} A / \Delta t$ is an equivalent drag matrix and is the stiffness contribution owing to the presence of the fluid [30,33]. A is a matrix that eliminates the rotational degrees of freedom from the global displacement vector Δd. Finally, invoking the arbitrariness of the virtual displacements and equating the internal (equation (A 11)) and the external virtual work (the sum of equations (A 13) and (A 18)) we obtain the following equation of motion for the FSI problem, which will be solved to obtain the incremental displacements (Δd) after incorporating the appropriate boundary conditions [30].

$$
(\underbrace{K_{\text{M}}^t + K_{\text{G}}^t}_{\text{solid}} + \underbrace{K_{\text{D}}^t}_{\text{fluid}}) \Delta d = F_{\text{ext}}^{t+\Delta t} - F_{\text{int}}^t. \tag{A 19}
$$

Appendix B. Dimensional analysis for the chiral micro-swimmers

Starting point for the dimensional analysis will be the virtual work expression, given by $\delta W_{\text{int}} = \delta W_{\text{ext}}$, see equations (A 6), (A 12) and (A 16), for a film of thickness h:

$$
\underbrace{\int (\delta \epsilon \cdot P + \delta \kappa \cdot M) \, dA}_{\text{elastic part}} = \underbrace{\int \delta u \cdot T_d \, dA}_{\text{viscous part}} - \underbrace{\int (N_x h \delta \beta_y - N_y h \delta \beta_x) \, dA}_{\text{magnetic part}}. \tag{B 1}
$$

Assuming the evolved chiral shape is mainly twisting dominated and the in-plane deformations are negligible, the above equation can be simplified into

$$\int_0^L \int_0^W \delta\kappa_{xy} M_{xy}\, dA = \int_0^L \int_0^W T_d \delta w\, dA - \int_0^{L_0} \int_0^W N_x h \delta\beta_y\, dA, \tag{B 2}$$

where $M_{xy} = (Gh^3/12)\kappa_{xy}$, $\kappa_{xy} = (\partial/\partial y)(\partial w/\partial x) - (\partial/\partial x)(\partial w/\partial y)$, G being the shear modulus, and L and W are the length and width of the film, respectively. As the film is partially magnetic, the magnetic body couple will only act on the magnetic portion (L_0) of the film. We now introduce dimensionless variables (.)* such that $x = X^*L$, $y = Y^*W$ and $A = A^*LW$ (or $A = A^*L_0W$ for the magnetic part). From the standard torsion formula, the twist angle follows to be $\theta_{\text{twist}} = TL/GJ$, with T and J being the applied torque and the second polar moment of area, respectively. As $J \propto Wh^3$ for rectangular cross sections, [42], $\theta_{\text{twist}} \propto L/W$ for a given value of the film thickness, which leads to $w \propto \theta_{\text{twist}}W \approx L$ or $w = W^*L$. Substitution yields the following pre-factors for the elastic, viscous and magnetic parts

$$\frac{Gh^3 L}{12W} \int_0^1 \int_0^1 \delta\kappa_{xy}^* \kappa_{xy}^*\, dA^* = T_d L^2 W \int_0^1 \int_0^1 \delta w^*\, dA^* - N_x h L L_0 \int_0^1 \int_0^1 \delta\beta_y^*\, dA^*. \tag{B 3}$$

It can be noted that the choice of the characteristic length in the x-direction is not the same for all integrals in the above equation, which leads to a governing dimensionless (length) parameter, L_0/L, defining the normalized length of the magnetic portion in the elastica. Normalization with the elastic term reveals the following governing dimensionless (force) parameters [32,33]: (i) the magnetic number, $M_n = 12N_x WL_0/Gh^2$, i.e. the ratio of magnetic to elastic forces, and (ii) the fluid number, $F_n = 12LW^2 T_d/Gh^3$, i.e. the ratio of fluid to elastic forces.[2] From dimensional considerations, T_d should scale with $\mu\dot{\theta}_{\text{twist}}$ or $\mu\omega L/W$, where μ is viscosity of the fluid and $\omega = 2\pi/t_{\text{cycle}}$ is the angular frequency of the magnetic field actuation. Thus, the final form of the three governing dimensionless parameters is as follows:

(i) the fraction of film that is magnetic,

$$\frac{L_0}{L}, \tag{B 4}$$

(ii) the magnetic number,

$$M_n = \frac{12N_x}{G}\frac{LW}{h^2}\frac{L_0}{L} = \frac{12MB}{G}\frac{LW}{h^2}\frac{L_0}{L}, \tag{B 5}$$

(iii) the fluid number,

$$F_n = \frac{12\mu\omega}{G}\frac{WL^2}{h^3}. \tag{B 6}$$

Note that F_n can be independently altered by changing the viscosity (μ) or frequency (ω). Similarly, M_n can be independently controlled with the remanent magnetization (M) or with the external magnetic field (B), which eventually influences the magnetic body couple (N_x).

Appendix C. Analytical study for chirality-induced propulsion

Resistive force theory suggested by Gray & Hancock [29] can be used to get the first-order approximation of the swimming velocity associated with the chirality-induced propulsion. As the chirality is induced owing to the twisting of the film, it can be assumed that the twist angle (θ) varies along the length of the micro-swimmer leading to a twist gradient of $(\theta_2 - \theta_1)/dx$ as shown in figure 9. Assuming that the local drag-coefficients for a chiral micro-swimmer are C_{dL}, C_{dW} and C_{dh} in the length, width and thickness direction, respectively, the x-component of total force on

---

[2]Note that the factor 12 can be removed without loss of generality. Here, we decide to keep it in for historical reasons.
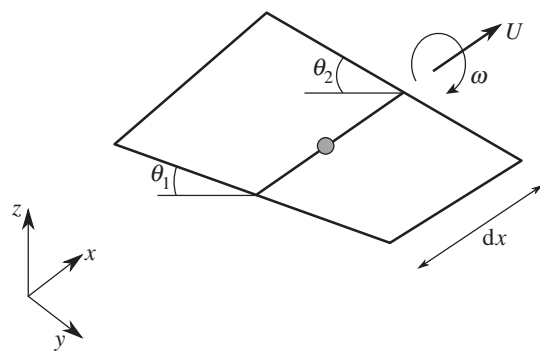
Figure 9. Illustration of the twist angle (θ) variation along the length of a chiral micro-swimmer. The micro-swimmer has a steady-state swimming velocity of magnitude U and is subjected to an external torque that has an angular frequency of ω.

the chiral micro-swimmer of length L and width W can be written as

$$\int_0^L \int_{-W/2}^{W/2} \mathrm{d}F_x \, \mathrm{d}x \, \mathrm{d}y, \tag{C1}$$

where,

$$\mathrm{d}F_x = C_{dh}\{U \sin\theta_y + \omega y \cos\theta_y\}\sin\theta_y + C_{dL}\{U\cos\theta_y - \omega y \sin\theta_y\}\cos\theta_y, \tag{C2}$$

with $\mathrm{d}F_x$ being the force acting on a segment of length $\mathrm{d}x$ and width $\mathrm{d}y$, and $\theta_y = y\,\mathrm{d}\theta/\mathrm{d}x$ is the developed helix or the pitch angle. Note that the propulsion force in the direction perpendicular to the plane of actuation (F_x) results from the difference of the viscous drag in the tangential and normal directions, C_{dL} and C_{dh}, respectively (see equation (C2)). The above expression is derived assuming that the micro-swimmer is swimming with a velocity U and is externally actuated with ω being the angular frequency of actuation (the angular frequency of the external magnetic field in this case; figure 9). In addition, the total force consists of a propulsive part owing to the actuation forces and a retarding part owing to the drag forces opposing the horizontal swimming velocity (the part associated with U). When the micro-swimmer reaches a steady-state swimming velocity U, the propulsive and retarding forces are in (dynamic) equilibrium, so that the total force must be zero [33].

For the general case of chirality-induced propulsion, we account for the nonlinear variation of twist angle by assuming a power-law relationship, $\theta = \theta_{\max}(x/L)^n$, where the power-law-exponent (n) quantifies the nonlinearity of the twist angle variation. We begin with obtaining a closed-form expression for the swimming velocity assuming a linear variation for the twist angle (i.e. $n = 1$) and considering only the first-order terms (i.e. higher order terms are neglected), which leads to

$$U = \frac{\omega\theta_{\max}W^2}{12L}\left(\frac{C_{dh}}{C_{dL}} - 1\right). \tag{C3}$$

The above expression suggests that the swimming velocity (U) scales linearly with the frequency of actuation ω and quadratically with the width of the film W. Additionally, the swimming velocity is directly proportional to the maximum twist gradient in the film $\theta_{\max}/L$. Next, we explore the influence of nonlinearity in the twist angle variation (i.e. $n \neq 1$) on the swimming velocity. Here, we consider the full form of the total force without neglecting the higher order terms and solve the equation numerically using Mathematica.[3] The results are shown in figure 10 for $U_{\text{normalized}} = U/U_{n=1}$, where we explicitly assume $C_{dh} = 2C_{dL}$. It can be clearly seen that the swimming velocity will be maximal when $n \approx 1$. In other words, the linear variation of the twist angle along the micro-swimmer length gives the maximal velocity for a given set of parameters ($\omega, \theta_{\max}, L$ and W). This can be interpreted in the following way. For the cases

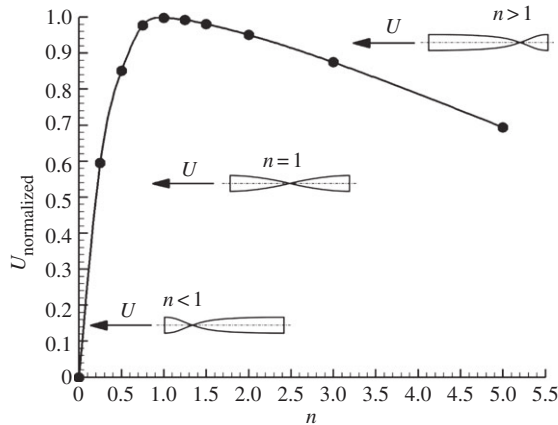[3]Mathematica is a trademark of Wolfram Research, Inc.

Figure 10. Influence of nonlinearity exponent (n) in the twist angle variation, $\theta = \theta_{\max}(x/L)^n$, on the swimming velocity, and $U_{\text{normalized}} = U/U_{n=1}$. The swimming velocity is maximum when $n \approx 1$. The illustrated cross ($\times$) on the micro-swimmer's image represents the location where $\theta = \theta_{\max}/2$.

of $n \approx 1$, the whole length of the micro-swimmer will be effectively used to generate propulsion as the twist gradient is uniform along the length. However, once we deviate from linearity ($n \neq 0$), the portion of the film having the maximum twist gradient is responsible for propulsion, while the rest of the film with a lower twist gradient (mainly) contributes to the opposing drag forces, which leads to a decrease in the swimming velocity. Note that the swimming velocity will be zero for $n = 0$ owing to reciprocal motion of the film in the absence of any twist gradient along the length.

Note that the analytical study does not provide a complete picture for the physical phenomenon. For instance, the elasticity of the film is not accounted for and the role of viscous and magnetic forces are not clearly distinguished. Nevertheless, it is interesting that such a simple analysis can give useful insights on the physics of the problem and can provide an accurate measure of the scaling $U \propto \omega\theta_{\max}W^2/L$.

References

1. Nelson BJ, Kaliakatsos IK, Abbott JJ. 2010 Microrobots for minimally invasive medicine. *Annu. Rev. Biomed. Eng.* **12**, 55–85. (doi:10.1146/annurev-bioeng-010510-103409)
2. Martel S *et al.* 2007 Automatic navigation of an untethered device in the artery of a living animal using a conventional clinical magnetic resonance imaging system. *Appl. Phys. Lett.* **90**, 114105. (doi:10.1063/1.2713229)
3. Gao W *et al.* 2012 Cargo-towing fuel-free magnetic nanoswimmers for targeted drug delivery. *Small* **8**, 460–467. (doi:10.1002/smll.201101909)
4. Wang J, Gao W. 2012 Nano/microscale motors: biomedical opportunities and challenges. *ACS Nano* **6**, 5745–5751. (doi:10.1021/nn3028997)
5. Fischer P, Ghosh A. 2011 Magnetically actuated propulsion at low Reynolds numbers: towards nanoscale control. *Nanoscale* **3**, 557–563. (doi:10.1039/c0nr00566e)
6. Martel S, Mohammadi M, Felfoul O, Lu Z, Pouponneau P. 2009 Flagellated magnetotactic bacteria as controlled MRI-trackable propulsion and steering systems for medical nanorobots operating in the human microvasculature. *Int. J. Robot. Res.* **28**, 571–582. (doi:10.1177/0278364908100924)
7. Guo S, Pan Q, Khamesee MB. 2008 Development of a novel type of microrobot for biomedical application. *Microsyst. Technol.* **14**, 307–314. (doi:10.1007/s00542-007-0430-1)
8. Kósa G, Jakab P, Székely G, Hata N. 2012 MRI driven magnetic microswimmers. *Biomed. Microdevices* **14**, 165–178. (doi:10.1007/s10544-011-9594-7)

9. Peyer KE, Zhang L, Nelson BJ. 2013 Bio-inspired magnetic swimming microrobots for biomedical applications. *Nanoscale* **5**, 1259–1272. (doi:10.1039/c2nr32554c)
10. Wang J, Manesh KM. 2010 Motion control at the nanoscale. *Small* **6**, 338–345. (doi:10.1002/smll.200901746)
11. Ebbens SJ, Howse JR. 2010 In pursuit of propulsion at the nanoscale. *Soft Matter* **6**, 726–738. (doi:10.1039/B918598D)
12. Purcell EM. 1977 Life at low Reynolds number. *Am. J. Phys.* **45**, 3–11. (doi:10.1119/1.10903)
13. Lauga E, Powers TR. 2009 The hydrodynamics of swimming microorganisms. *Rep. Progr. Phys.* **72**, 096601. (doi:10.1088/0034-4885/72/9/096601)
14. Dreyfus R, Baudry J, Roper ML, Fermigier M, Stone HA, Bibette J. 2005 Microscopic artificial swimmers. *Nature* **437**, 862–865. (doi:10.1038/nature04090)
15. Garstecki P, Tierno P, Weibel DB, Sagués F, Whitesides GM. 2009 Propulsion of flexible polymer structures in a rotating magnetic field. *J. Phys. Condens. Matter* **21**, 204110. (doi:10.1088/0953-8984/21/20/204110)
16. Zhang L, Peyer KE, Nelson BJ. 2010 Artificial bacterial flagella for micromanipulation. *Lab Chip* **10**, 2203–2215. (doi:10.1039/C004450B)
17. Ishiyama K, Sendoh M, Yamazaki A, Arai KI. 2001 Swimming micro-machine driven by magnetic torque. *Sens. Actuators A Phys.* **91**, 141–144. (doi:10.1016/S0924-4247(01)00517-9)
18. Manghi M, Schlagberger X, Netz RR. 2006 Propulsion with a rotating elastic nanorod. *Phys. Rev. Lett.* **96**, 068101. (doi:10.1103/PhysRevLett.96.068101)
19. Li H, Tan J, Zhang M. 2009 Dynamics modeling and analysis of a swimming microrobot for controlled drug delivery. *Autom. Sci. Eng., IEEE Trans.* **6**, 220–227. (doi:10.1109/TASE.2008.917137)
20. Tierno P, Golestanian R, Pagonabarraga I, Sagués F. 2008 Magnetically actuated colloidal microswimmers. *J. Phys. Chem. B* **112**, 16 525–16 528. (doi:10.1021/jp808354n)
21. Qian B, Powers TR, Breuer KS. 2008 Shape transition and propulsive force of an elastic rod rotating in a viscous fluid. *Phys. Rev. Lett.* **100**, 078101. (doi:10.1103/PhysRevLett.100.078101)
22. Abbott JJ, Peyer KE, Lagomarsino MC, Zhang L, Dong L, Kaliakatsos IK, Nelson BJ. 2009 How should microrobots swim? *Int. J. Robot. Res.* **28**, 1434–1447. (doi:10.1177/0278364909341658)
23. Ghosh A, Fischer P. 2009 Controlled propulsion of artificial magnetic nanostructured propellers. *Nano Lett.* **9**, 2243–2245. (doi:10.1021/nl900186w)
24. Zhang L, Abbott JJ, Dong L, Kratochvil BE, Bell D, Nelson BJ. 2009 Artificial bacterial flagella: fabrication and magnetic control. *Appl. Phys. Lett.* **94**, 064107. (doi:10.1063/1.3079655)
25. Coq N, du Roure O, Fermigier M, Bartolo D. 2009 Helical beating of an actuated elastic filament. *J. Phys. Condens. Matter* **21**, 204109. (doi:10.1088/0953-8984/21/20/204109)
26. Peyer K, Qiu F, Zhang L, Nelson B. 2012 Movement of artificial bacterial flagella in heterogeneous viscous environments at the microscale. In *IEEE/RSJ Int. Conf. on Intelligent Robots and Systems (IROS), 2012, Vilamoura, Algarve, Portugal, 7–12 October 2012*, pp. 2553–2558. New York, NY: IEEE.
27. Tottori S, Zhang L, Qiu F, Krawczyk KK, Franco-Obregón A, Nelson BJ. 2012 Magnetic helical micromachines: fabrication, controlled swimming, and cargo transport. *Adv. Mater.* **24**, 811–816. (doi:10.1002/adma.201103818)
28. Purcell EM. 1997 The efficiency of propulsion by a rotating flagellum. *Proc. Natl Acad. Sci. USA* **94**, 11 307–11 311. (doi:10.1073/pnas.94.21.11307)
29. Gray J, Hancock GJ. 1955 The propulsion of sea-urchin spermatozoa. *J. Exp. Biol.* **32**, 802–814.
30. Khaderi SN, Onck PR. 2012 Fluid–structure interaction of three-dimensional magnetic artificial cilia. *J. Fluid Mech.* **708**, 303–328. (doi:10.1017/jfm.2012.306)
31. Namdeo S, Khaderi SN, Onck PR. 2013 Swimming dynamics of bi-directional artificial flagella. *Phys. Rev. E* **88**, 043013. (doi:10.1103/PhysRevE.88.043013)
32. Khaderi SN, Baltussen MGHM, Anderson PD, Ioan D, den Toonder JMJ, Onck PR. 2009 Nature-inspired microfluidic propulsion using magnetic actuation. *Phys. Rev. E* **79**, 046304. (doi:10.1103/PhysRevE.79.046304)
33. Namdeo S, Khaderi SN, den Toonder JMJ, Onck PR. 2011 Swimming direction reversal of flagella through ciliary motion of mastigonemes. *Biomicrofluidics* **5**, 034108. (doi:10.1063/1.3608240)
34. Babataheri A, Roper M, Fermigier M, Roure OD. 2011 Tethered fleximags as artificial cilia. *J. Fluid Mech.* **678**, 5–13. (doi:10.1017/S002211201100005X)
35. van Oosten CL, Bastiaansen CWM, Broer DJ. 2009 Printed artificial cilia from liquid-crystal network actuators modularly driven by light. *Nat. Mater.* **8**, 677–682. (doi:10.1038/nmat2487)

36. Belardi J, Schorr N, Prucker O, Rühe J. 2011 Artificial cilia: Generation of magnetic actuators in microfluidic systems. *Adv. Funct. Mater.* **21**, 3314–3320. (doi:10.1002/adfm.201100787)
37. Hussong J, Schorr N, Belardi J, Prucker O, Rühe J, Westerweel J. 2011 Experimental investigation of the flow induced by artificial cilia. *Lab Chip* **11**, 2017–2022. (doi:10.1039/C0LC00722F)
38. Khaderi SN *et al.* 2011 Magnetically-actuated artificial cilia for microfluidic propulsion. *Lab Chip* **11**, 2002–2010. (doi:10.1039/C0LC00411A)
39. Bathe KJ, Ho LW. 1981 A simple and effective element for analysis of general shell structures. *Comput. Struct.* **13**, 673–681. (doi:10.1016/0045-7949(81)90029-8)
40. Allman DJ. 1984 A compatible triangular element including vertex rotations for plane elasticity analysis. *Comput. Struct.* **19** (special memorial issue), 1–8. (doi:10.1016/0045-7949(84)90197-4)
41. Pozrikidis C. 2002 *A practical guide to boundary element methods*. London, UK: Chapman & Hall/CRC.
42. Ugural AC, Fenster SK. 2003 *Advanced strength and applied elasticity*. Upper Saddle River, NJ: Prentice Hall.

18

rspa.royalsocietypublishing.org *Proc. R. Soc. A* **470**: 20130547